Computers and Fluids 232 (2022) 105189

Contents lists available at ScienceDirect

Computers and Fluids

journal homepage: www.elsevier.com/locate/compfluid

Application of projection methods to simulating mass transport in reverse osmosis systems

Jacob Johnston, Jincheng Lou, Nils Tilton [*]

Mechanical Engineering, Colorado School of Mines, United States of America

ARTICLE INFO

Keywords:
Reverse osmosis
CFD
Boundary conditions
Membrane
Finite volume methods
Projection methods

ABSTRACT

Reverse Osmosis has important applications to seawater desalination and advanced water treatment. Its efficiency depends, however, on unsteady fluid flow and solute transport that are challenging to simulate. The challenges arise due to interactions between solute boundary layers and unsteady vortical flow structures generated by complicated geometries. These flow structures also interact with semi-permeable membranes through which the permeate flow depends on the local pressure. We show that this additional pressure coupling causes the temporal accuracy of traditional projection methods to drop to first-order. We track the source of this accuracy drop to the treatment of viscous terms in the derivation of the Poisson equation used to update the velocity and pressure fields. This allows us to propose a modified projection method that recovers second-order temporal accuracy. Finally, we show that the modified projection method can be coupled to convective outlet conditions and immersed boundary conditions to simulate reverse osmosis in steady and unsteady flow regimes.

1. Introduction

Reverse osmosis (RO) plays a key role in the water–energy–climate nexus due to its applications to desalination and wastewater treatment [1,2]. The energy efficiency of RO systems depend, however, on unsteady fluid flow and solute transport that are challenging to observe experimentally or simulate numerically. The numerical challenges arise because RO systems include unsteady vortical flow structures generated by bluff bodies with complicated geometries. These flow structures also interact with semipermeable membranes through which the fluid velocity is a function of the local pressure on the membrane. This additional pressure–velocity coupling is not straightforward to apply, particularly when RO systems are simulated using projection methods. Projection methods are the preferred method of simulating unsteady incompressible fluid flows, because they are efficient, non-iterative, and produce second-order spatial and temporal accuracy for the velocity field when implemented using classic finite-volume methods [3]. Their accuracy for the pressure field, however, can be as low as first-order [4–6]. The current study shows that this issue is important for RO, because the velocity–pressure coupling on the membrane causes the accuracy of the velocity field to also drop to first-order. A final challenge arises because mass exits RO systems through both an outlet and membrane. Due to the dependence of the transmembrane flow on the pressure, the mass flow rates exiting the membrane and outlet are not known at the beginning of each time step. This complicates the application of mass-conserving boundary conditions.

The current study addresses these issues using semi-implicit projection methods and immersed boundary methods. Fig. 1(*a*) shows the geometry of typical “plate-and-frame” RO systems used in bench-scale experiments. A high-pressure feed solution of water and solutes enters from the left ($x = 0$) and flows beneath an impermeable flat plate and above a semi-permeable membrane sheet. The plate and membrane are separated by a channel height h, typically around 1 mm. The pressure difference between the high-pressure feed and low-pressure permeate opposite the membrane drives water through the membrane while blocking most solutes. To simplify the presentation of our methods, we hereinafter assume “complete solute rejection” such that the solute concentration of the permeate is zero. In practice, RO systems often reject around 98% of solutes [7]. Typical feed pressures vary between 10 to 80 bar, while the permeate pressure is often near atmospheric. The coupling between the transmembrane permeate velocity and the pressure field is often modelled using the following Darcy-type boundary condition,

$$v_m(x,z,t) = \kappa\left[p_m(x,z,t) - p_p - \Pi(x,z,t)\right], \tag{1}$$

where κ is the membrane permeance (SI units $\mathrm{ms^{-1}Pa^{-1}}$), v_m is the velocity of the local transmembrane flow, p_m is the local pressure on

---

[*] Corresponding author.
E-mail address: ntilton@mines.edu (N. Tilton).

https://doi.org/10.1016/j.compfluid.2021.105189
Received 10 June 2021; Received in revised form 9 September 2021; Accepted 1 October 2021

Nomenclature

β	Blockage ratio $\beta = D_c/h$
Δt	Time step (s)
κ	Membrane permeance (m/s Pa)
$\mathbf{n}$	Unit normal to surfaces
$\mathbf{u}$	Velocity vector (m/s)
$\mathbf{u}^*$	Provisional velocity vector in projection method (m/s). See Eq. (17)
$\mathcal{D}$	Mass diffusivity (m^2/s)
μ	Dynamic viscosity (Pa s)
ω	Frequency (1/s)
ϕ	Intermediate variable used in projection method. See Eq. (20)
Π	Osmotic pressure $\Pi = Ac$ (Pa)
ρ	Density (kg/m^3)
A	Osmotic pressure constant (Pa l/ g)
c	Concentration (g/l)
C_m	Membrane surface concentration (g/l)
C_{in}	Feed concentration (g/l)
D_c	Cylinder diameter (m)
h	Channel height (m)
j_v	Average transmembrane permeate flux (LMH)
L	Channel length (m)
p	Pressure (Pa)
Re	Reynolds number $Re = U_{in}h/\nu$
t	Time (s)
u, v	Velocity component along x and y coordinates (m/s)
U_{in}	Inlet velocity (m/s)
v_m	Velocity through the membrane (m/s)
x, y	Cartesian coordinates (m)
x_c, y_c	Cylinder position (m). See Fig. 2
LMH	Litre per metre squared per hour (l/m^2 h)
P_{out}	Outlet pressure
Re_c	Critical Reynolds number for transition to vortex shedding
RO	Reverse osmosis
TVD	Total variation diminishing

the membrane feed surface, p_p is the permeate pressure, and Π is the osmotic pressure. Eq. (1) is written so that v_m is positive when permeate exits the feed channel. We stress that v_m, p_m, and Π all vary along the membrane surface. Pressure variations in the permeate, however, are often negligible, and p_p is usually set to the reference value $p_p = 0$ for convenience. Note that the permeance κ differs from the permeability k used in the classical Darcy equation [8]. The two are related by $\kappa = k/(\mu d)$, where μ and d are the feed viscosity and membrane thickness, respectively. The osmotic pressure is often approximated as $\Pi = Ac$, where c is the solute concentration and A is a constant of proportionality. More general quadratic or cubic polynomials can also be determined [9].

RO is an inherently energy intensive process because the feed pressure must exceed the osmotic pressure to force permeate through the membrane. Moreover, the osmotic pressure at the membrane surface is often much higher than that of the incoming feed. This is due to concentration polarization, which refers to solute accumulation adjacent to the membrane surface, as illustrated in Fig. 1(*a*). Polarization occurs because solutes are advected towards the membrane where they form a thin boundary layer in which there is a large increase in solute concentration. Concentration polarization is a serious technical challenge for RO because it increases the required operating pressure and reduces the fraction of water recovered from the feed. It also leads to mineral scaling, which is the precipitation of solutes onto the membrane surface. This impedes filtration, reduces membrane life, and increases maintenance costs.

Concentration polarization in RO is further complicated by the presence of feed spacers. These are plastic mesh-like materials placed in the feed channel to support the membrane and provide space for feed flow tangential to the membrane , as sketched in Fig. 1(*b*). In plate-and-frame systems, feed spacers separate the membrane from the opposing flat plate. In industrial systems, the plate is replaced with a second membrane. In addition to separating membranes, feed spacers play an important role in polarization and mineral scaling by generating regions of preferential solute accumulation and precipitation on the membrane surface [10–21]. The fundamental mechanics of this process, however, are not fully understood.

Numerous CFD studies have made important contributions to simulating RO. For reviews, we refer readers to [22–24]. Here, we focus on simulations of RO systems with feed spacers. Due to the numerical challenges, simulations of feed channels with spacers often replace the membrane with an impermeable wall [25–37]. This approach is useful for studying the effects of spacer geometry on membrane shear stresses and downstream pressure drops. Other studies include transmembrane flow and concentration polarization, but for operating conditions that produce steady or quasi-steady feed flow [35,38–40]. Such studies have advanced our understanding of biofouling [35,38] and mineral scaling [39,40]. The current study is motivated by the fact that RO systems typically operate for feed Reynolds numbers in the range $10 \leq Re \leq 1000$, where $Re = \rho U_{in} h/\mu$ is defined using the mean inlet velocity U_{in} and density ρ. For this range, studies suggest that spacer filaments generate unsteady vortex shedding or even turbulence [41,42], though the Reynolds numbers for these transitions are not fully understood. Further studies suggest that vortex shedding plays an important role in polarization [27,43–46]. The development of an efficient projection method for simulating unsteady flow in RO would provide an important tool for studying the transition to vortex shedding and its impacts on polarization. It would also help address the broader issue that published

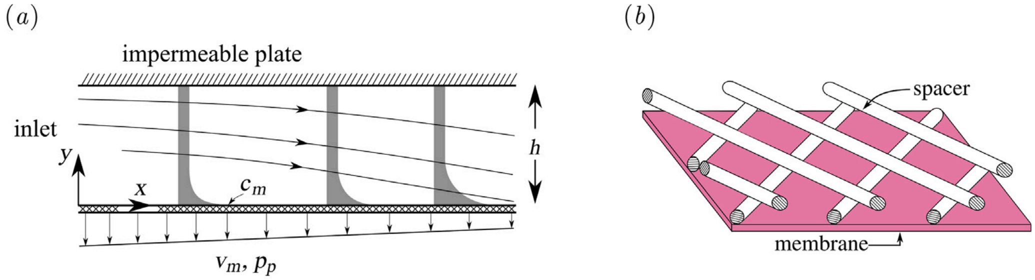

Fig. 1. (*a*) Sketch (not to scale) of a plate-and-frame RO system. Feed enters at $x = 0$ and flows between an impermeable plate at $y = h$ and a semi-permeable membrane at $y = 0$. Concentrate exits the channel downstream at $x = L$. The formation of a concentration polarization layer is shown in grey. (*b*) Sketch (not to scale) of feed spacers.

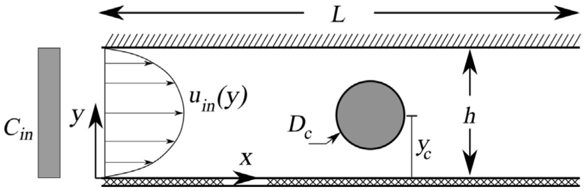

Fig. 2. Sketch (not to scale) of the 2-D RO flow channel with a spacer considered in this study. Solution enters the channel with concentration C_{in} and mean velocity U_{in}. The spacer has a diameter D_c.

simulations of RO rarely detail how they implement membrane and outlet conditions, and rarely demonstrate the order-of-accuracy of their methods.

Thus motivated, the current study explores the application of two projection methods to RO. We begin with the classical method of Bell et al. [3]. For fluid systems with Dirichlet velocity conditions on all boundaries, this method produces second-order spatial–temporal accuracy for the velocity field, but can produce lower accuracy for the pressure. We then consider a class of projection methods proposed by Kim and Moin [47], Brown et al. [4], and Guy and Fogelson [5] that try to increase the accuracy of the pressure to second order [6]. We explore the spatial and temporal accuracy of both approaches using manufactured solutions. We first explore how the treatment of inlet and outlet conditions affect conservation of mass, mesh-independence, and flow structures exiting the domain. Finally, we use the methods to simulate RO systems with unsteady vortex shedding generated by a single spacer filament. The filament is simulated using recent immersed boundary methods detailed in Lou et al. [41].

The remaining study is organized as follows. Section 2 presents the geometry and governing equations. Section 3 investigates the projection methods. Section 4 explores the application of inlet and outlet conditions. Section 5 applies our methods to simulations of unsteady vortex shedding in an RO system with a single spacer filament. Section 6 presents our conclusions.

2. Problem formulation and discretization

We consider the incompressible flow of a Newtonian fluid in a 2D plate-and-frame RO system of length L and channel height h, as sketched in Fig. 2. A cylindrical spacer filament of diameter D_c is located at $(x, y) = (x_c, y_c)$. Feed enters the system at $x = 0$ with a uniform concentration C_{in} and mean velocity U_{in}. At the channel outlet, $x = L$, we fix the pressure to P_{out}. This mimics bench-scale RO systems that control the inlet feed rate using a positive displacement pump and that set the outlet pressure using a back pressure regulator.

2.1. Governing equations

Fluid flow in the feed channel is governed by the incompressible Navier–Stokes and continuity equations

$$\rho\left(\frac{\partial \mathbf{u}}{\partial t} + \mathbf{u}\cdot\nabla\mathbf{u}\right) = -\nabla p + \mu\nabla^2\mathbf{u} + \mathbf{b}, \tag{2}$$

$$\nabla\cdot\mathbf{u} = 0, \tag{3}$$

where $\mathbf{u} = [u\ v]$ is the velocity vector. The body force $\mathbf{b}$ is added for benchmarking performed in Section 3. We consider solute transport governed by the advection–diffusion equation

$$\frac{\partial c}{\partial t} + \mathbf{u}\cdot\nabla c = \mathcal{D}\nabla^2 c + q, \tag{4}$$

where $\mathcal{D}$ is the effective mass diffusion coefficient and c is measured in grams of solute per litre of water. The source term q is again added for benchmarking. Variations of thermo-physical properties are typically on the order of 1% [9] for the system lengths considered here. We consequently neglect them to simplify our presentation. They can nevertheless be included as demonstrated in Lou et al. [48]. We set $\rho, \mu, \mathcal{D}$ to those evaluated at the inlet conditions using relations (A.1)–(A.3) in Appendix A. These assume an inlet feed temperature of $T_{in} = 25$ °C.

At the inlet, we apply a uniform concentration C_{in} and fully-developed laminar velocity profile with mean velocity U_{in},

$$c\Big|_{x=0} = C_{in}, \quad u\Big|_{x=0} = 6U_{in}\left[\frac{y}{h} - \frac{y^2}{h^2}\right], \quad \frac{\partial v}{\partial x}\Big|_{x=0} = 0. \tag{5}$$

At the outlet, we apply the convective conditions [49]

$$\left[\frac{\partial f}{\partial t} + U_{in}\frac{\partial f}{\partial x}\right]_{x=L} = 0, \tag{6}$$

where $f = [u, v, c]$. On the upper plate and spacer surface, we apply the no-slip, no-penetration, and no flux conditions

$$u = v = \mathbf{n}\cdot\nabla c = 0,$$

where $\mathbf{n}$ is the unit normal to the surface. On the membrane at $y = 0$, the tangential velocity satisfies the no-slip condition ($u = 0$), which is well established for RO membranes. The transmembrane velocity (v) satisfies the Darcy condition (1) with $p_p = 0$. To simplify the presentation of our methods, we approximate the osmotic pressure as $\Pi = Ac$, though higher-order polynomial approximations pose no challenge. The Darcy condition (1) can then be written as

$$v\Big|_{y=0} = -\kappa\Big[p - Ac\Big]_{y=0} + s, \tag{7}$$

where s is an added source term that is zero, except for benchmarking purposes discussed in Section 3. We determined the osmotic pressure constant $A = 77{,}170$ Pa l/g by performing a linear fit to the Harvie–Moller–Weare formulation of the Pitzer model [50]. This value produces a relative error below 1% when $0 \le c \le 100$ g/l. Assuming no transmembrane solute flux (called “complete rejection” in the membrane community) requires solute advection and diffusion normal to the membrane to sum to zero,

$$\left[vc - \mathcal{D}\frac{\partial c}{\partial y}\right]_{y=0} = \gamma, \tag{8}$$

where γ is an added source term for benchmarking purposes. Consideration of partial rejection is straightforward, but neglected here for brevity.

2.2. Discretization of governing equations

We discretize the governing equations (2)–(4) spatially using standard second-order finite-volume methods on a staggered grid [51], as sketched in Fig. 3(a). The velocities u (squares) and v (triangles) are stored on cell faces, while p and c are stored at cell centroids (solid dots). In our presentation below, we assume a uniform grid to simplify our discussion. The discretization for non-uniform grids is provided in Appendix B.

Consider the x-component of the Navier–Stokes Eqs. (2) in control volume form,

$$\rho\int_{CV}\frac{\partial u}{\partial t}dV + \int_{CS}\rho u(\mathbf{u}\cdot\mathbf{n})ds = \int_{CV}\left[-\frac{\partial p}{\partial x} + \mu\nabla^2 u + b^x\right]dV, \tag{9}$$

where CV and CS are the control volume and surface, respectively, shaded grey in Fig. 3(b), and b^x is the x-component of $\mathbf{b}$. We discretize the volume integrals as

$$\rho\int_{CV}\frac{\partial u}{\partial t}dV = \rho\frac{\partial u_P}{\partial t}dx\,dy, \tag{10}$$

$$\int_{CV}\left[-\frac{\partial p}{\partial x} + \mu\nabla^2 u + \mathbf{b}^x\right]dV = \left[-\frac{p_e - p_w}{dx} + \mu\nabla_d^2 u + b_p^x\right]dx\,dy, \tag{11}$$

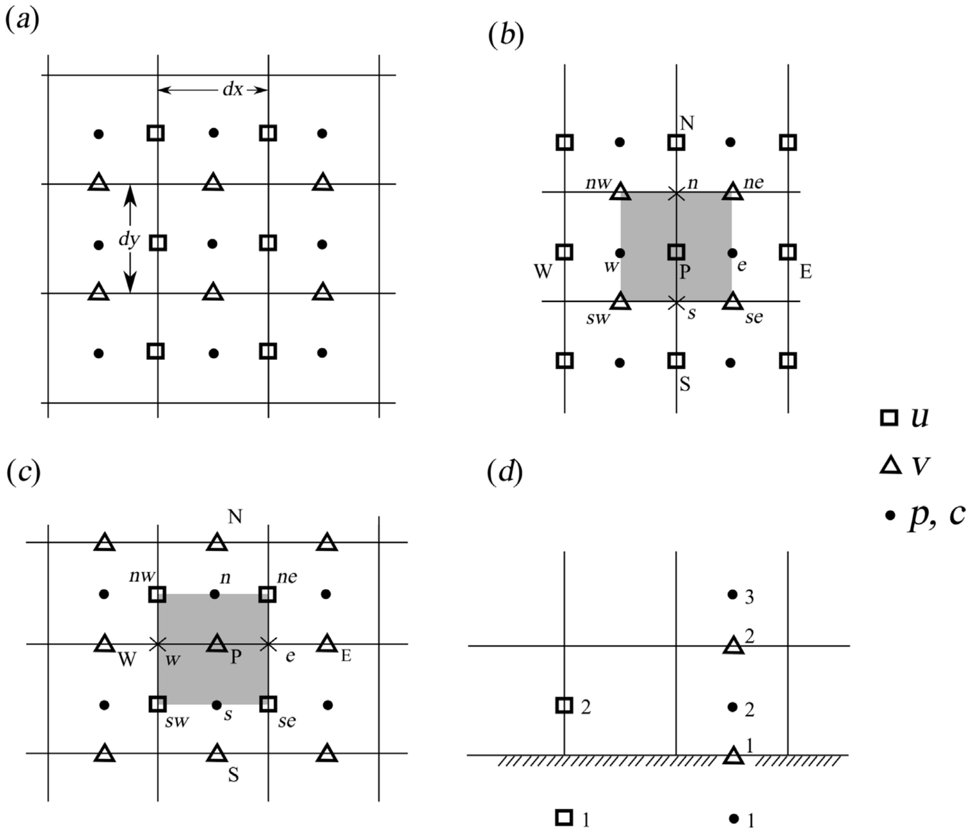

Fig. 3. (*a*) Sketch of the staggered grid. The flow fields u, v, p, and c are stored at the locations marked with squares, triangles, and solid dots, respectively. (*b*) The control volume (shaded grey) for discretizing the x-component of the Navier–Stokes equations. The locations n and s marked with cross symbols are not actual grid points. (*c*) The control volume used to discretize the y-component of the Navier–Stokes. (*d*) Application of boundary conditions using ghost nodes.

where $\nabla_d^2 u$ is the centred difference approximation

$$\nabla_d^2 u = \frac{u_W - 2u_P + u_E}{dx^2} + \frac{u_S - 2u_P + u_N}{dy^2}. \tag{12}$$

The subscripts denote evaluation of u, v, and p at the corresponding points labelled in Fig. 3(*b*). The advection term is discretized as

$$\int_{CS} \rho u(\mathbf{u}\cdot\mathbf{n})ds = \dot{m}_e u_e + \dot{m}_n u_n - \dot{m}_w u_w - \dot{m}_s u_s, \tag{13}$$

where $\dot{m}_e = \rho u_e dy$, $\dot{m}_w = \rho u_w dy$, $\dot{m}_n = \rho v_n dx$, and $\dot{m}_s = \rho v_s dx$. For now, we assume all velocities in Eq. (13) are approximated using standard centred differences, such as $u_e = (u_P + u_E)/2$ and $v_n = (v_{nw} + v_{ne})/2$. In Section 4, however, we report that outlet noise can be attenuated by discretizing advection terms with a TVD scheme.

The y-component of the Navier–Stokes equations is discretized as demonstrated above, using the control volume illustrated in Fig. 3(*c*). We then discretize the Navier–Stokes equations semi-implicitly in time using the second-order backwards Euler method for the linear terms and second-order Adams–Bashforth extrapolation for the nonlinear terms [51,52]. The discretized Navier–Stokes equations can then be written as

$$\rho\frac{3\mathbf{u}_P^{n+1} - 4\mathbf{u}_P^{n} + \mathbf{u}_P^{n-1}}{2\Delta t} + 2\mathbf{NL}^n - \mathbf{NL}^{n-1} = -\nabla_d p^{n+1} + \mu\nabla_d^2\mathbf{u}^{n+1} + b^{n+1}, \tag{14}$$

$$\nabla_d p = \left[\frac{p_e - p_w}{dx}\right]\mathbf{i} + \left[\frac{p_n - p_s}{dy}\right]\mathbf{j},$$

where $\mathbf{i}$ and $\mathbf{j}$ are unit vectors in the x and y directions, respectively, Δt is the time step, the superscript n denotes time $t = n\Delta t$, **NL** refers to the nonlinear advection term, and ∇_d is the discretized gradient operator. We use the backwards Euler method because it discretizes the pressure at the current time step, p^{n+1}. In contrast, the popular Crank–Nicholson method discretizes the pressure at an intermediate time $p^{n+1/2}$, which is inconsistent with the discretization of the Darcy membrane condition in Eq. (16) below.

The boundary conditions on the spacer surfaces are applied using the second-order immersed boundary method detailed in Lou et al. [41]. Boundary conditions on the inlet, outlet, plate, and membrane are applied using ghost nodes. To demonstrate, suppose we wish to apply the Robin conditions $au + b\partial u/\partial y = g_u$ and $av + b\partial v/\partial y = g_v$ on the boundary sketched in Fig. 3(*d*). We discretize these as

$$a\left[\frac{u_2^{n+1} + u_1^{n+1}}{2}\right] + b\left[\frac{u_2^{n+1} - u_1^{n+1}}{dy}\right] = g_u, \quad av_1 + b\left[\frac{v_2^{n+1} - v_1^{n+1}}{dy}\right] = g_v. \tag{15}$$

The membrane condition (8) for the solute is discretized as

$$D\left[\frac{c_2^{n+1} - c_1^{n+1}}{dy}\right] = 2v_1^n c_m^n - v_1^{n-1} c_m^{n-1}, \quad c_m = \frac{c_1 + c_2}{2},$$

where the subscripts denote the locations marked in Fig. 3(*d*) and we approximate the nonlinear term explicitly, using Adams–Bashforth extrapolation. The Darcy condition (1) is discretized as

$$v_1^{n+1} = -\kappa\left(p_m^{n+1} - Ac_m^{n+1}\right), \quad p_m = \frac{3}{2}p_2 - \frac{1}{2}p_3. \tag{16}$$

Note that we extrapolate p_m from the interior grid points because projection methods can produce nonphysical pressures at ghost nodes [5]. Implementation of these conditions in our projection methods is discussed in Section 3. We delay discussion of outlet conditions to Section 4.

3. Projection methods

We consider two projection methods for estimating p^{n+1} in the discretized Navier–Stokes Eq. (14). The first is that of Bell et al. [3], which we refer to as the "*base method*". The second is similar to those proposed by Kim and Moin [47], Brown et al. [4], and Guy and Fogelson [5], which we refer to as the "*improved method*". Both methods begin by solving the incremental equation

$$\rho \frac{3\mathbf{u}^* - 4\mathbf{u}^n + \mathbf{u}^{n-1}}{2\Delta t} + 2\mathbf{NL}^n - \mathbf{NL}^{n-1} = -\boldsymbol{\nabla}_d p^n + \mu \nabla_d^2 \mathbf{u}^* + \mathbf{b}^{n+1}, \tag{17}$$

where $\mathbf{u}^*$ estimates $\mathbf{u}^{n+1}$ using the pressure p^n from the previous time step. Subtracting Eq. (17) from Eq. (14), we find that

$$\mathbf{u}_P^{n+1} = \mathbf{u}_P^* - \alpha \boldsymbol{\nabla}_d \phi + \alpha \mu \nabla_d^2 \left(\mathbf{u}_P^{n+1} - \mathbf{u}_P^*\right), \tag{18}$$

where $\alpha = 2\Delta t / 3\rho$, and

$$\phi = p^{n+1} - p^n. \tag{19}$$

3.1. The base method

The projection method of Bell et al. neglects the viscous term in (18), so that

$$\mathbf{u}_P^{n+1} = \mathbf{u}_P^* - \alpha \boldsymbol{\nabla}_d \phi. \tag{20}$$

To determine an equation for ϕ, we consider the pressure cell shaded grey in Fig. 4(a), on which we discretize the continuity Eq. (3) as

$$\frac{u_e^{n+1} - u_w^{n+1}}{dx} + \frac{v_n^{n+1} - v_s^{n+1}}{dy} = 0. \tag{21}$$

Substituting Eq. (20) into the discretized continuity equation produces

$$\nabla_d^2 \phi = \frac{1}{\alpha} \left[\frac{u_e^* - u_w^*}{dx} + \frac{v_n^* - v_s^*}{dy} \right], \tag{22}$$

which is the well-known discretized Poisson equation $\nabla^2 \phi = (\boldsymbol{\nabla} \cdot \mathbf{u}^*)/\alpha$.

Choosing boundary conditions for ϕ is a topic of considerable discussion [4–6,49,53]. Suppose we wish to apply the Dirichlet condition $\mathbf{u}^{n+1} = \mathbf{u}_b$ on the boundary sketched in Fig. 4(b). It is now well established in the literature [3–5] that we can begin by applying $\mathbf{u}^* = \mathbf{u}_b$ when solving for the intermediate velocity. Eq. (20) then requires us to set $\phi_S = \phi_P$ in Fig. 4(b) to ensure that $v_s^{n+1} = v_b$. This is equivalent to applying $\partial\phi/\partial y = 0$ on the lower boundary. In summary, Dirichlet conditions are applied by setting

$$\mathbf{u}^* = \mathbf{u}_b, \quad \mathbf{n} \cdot \boldsymbol{\nabla} \phi = 0, \tag{23}$$

where $\mathbf{n}$ is the unit normal to the boundary.

To apply the Darcy membrane condition, we begin each time step by solving the advection–diffusion Eq. (4) for the concentration field c^{n+1}. We then apply the membrane condition to v_s^* in Fig. 4(b) as

$$v_s^* = -\kappa \left(\frac{3}{2} p_P^n - \frac{1}{2} p_N^n - A c_m^{n+1} \right), \tag{24}$$

using p^n because p^{n+1} is still unknown. To determine the required membrane condition for ϕ, we subtract condition (24) from the desired membrane condition for v_s^{n+1}

$$v_s^{n+1} = -\kappa \left(\frac{3}{2} p_P^{n+1} - \frac{1}{2} p_N^{n+1} - A c_m^{n+1} \right). \tag{25}$$

With the help of Eq. (20), this produces the following boundary condition for ϕ^{n+1},

$$\frac{\phi_P - \phi_S}{dy} - \frac{\kappa}{\alpha} \left(\frac{3}{2} \phi_P - \frac{1}{2} \phi_N \right) = 0. \tag{26}$$

This is equivalent to the Robin condition $\partial\phi/\partial y - (\kappa/\alpha)\phi = 0$. Though this condition can be derived in a continuous sense, the discrete derivation explains that $\partial\phi/\partial y$ must be approximated using a centred difference, while $(\kappa/\alpha)\phi$ must be extrapolated. Note that when $\kappa = 0$, condition (26) recovers condition (23) for an impermeable wall.

To explore the accuracy of the base method, we consider the manufactured solution,

$$\begin{aligned} u_e &= \sin(x)\cos(y)\cos(\omega t), \\ v_e &= -\cos(x)\sin(y)\cos(\omega t) - \kappa \sin(x)\cos(\omega t), \\ p_e &= \sin(x)\sin(y)\cos(\omega t) + \sin(x)\cos(\omega t), \\ c_e &= \cos(x)\cos(y)\cos(\omega t), \end{aligned} \tag{27}$$

in the domain $(x, y) \in (0, 2\pi) \times (0, 2\pi)$, with a membrane on the lower boundary ($y = 0$). Solution (27) satisfies the governing equations (2)–(4) and membrane boundary conditions (7)–(8) with the addition of appropriate forcing terms b, q, s, and γ. The solution is steady when $\omega = 0$ and unsteady otherwise. On the left ($x = 0$) and right ($x = 2\pi$) boundaries, we apply $\mathbf{u} = \mathbf{u}_e$ and $c = c_e$. On the top boundary, we apply $\mathbf{u} = \mathbf{u}_e$ and $\partial c/\partial y = \partial c_e/\partial y$.

We test the spatial accuracy by setting $\omega = 0$ and integrating from $\mathbf{u}^0 = p^0 = c^0 = 0$ to steady-state using N finite-volumes in each direction. We then measure the relative error of each field as,

$$Err_N = \frac{\|f_e - f_N\|_\infty}{\|f_e\|_\infty}, \tag{28}$$

where f_e and f_N are the exact and numerical solutions, respectively. We found that the base method is spatially second-order accurate for all variables. The results are not shown for brevity.

We test the temporal accuracy by setting $\omega = 2\pi$ and integrating from $t = 0$ to $t = 1$ using exact initial conditions. To isolate the temporal error, we use the approach of Karam et al. [54]. We first calculate a reference solution f_{ref} for which the temporal error is negligible in comparison to the spatial error. For that, we use the small time step $\Delta t = 10^{-5}$. We then define the temporal error as

$$Err_t = \frac{\|f_t - f_{ref}\|_\infty}{\|f_{ref}\|_\infty}, \tag{29}$$

where f_t is the solution using the larger time step $\Delta t > 10^{-5}$ and the same spatial resolution as f_{ref}. This definition of Err_t removes the spatial error and isolates the temporal error.

We evaluate the temporal accuracy for the permeances $\kappa = 0, 0.001$, and 0.01, such that the simulated velocity through the membrane is 0%, 0.1%, or 1% of the maximum velocity. These produce challenging test cases compared to traditional RO systems for which the transmembrane velocity is typically five orders of magnitude smaller than the inlet feed velocity. When $\kappa = 0$, there is no coupling between the pressure and the velocity, and we found that the velocity maintains second-order accuracy in time. When κ is non-zero, however, the temporal accuracy of the base method is less than second-order for all variables. Fig. 5(a) shows that when $\kappa = 0.01$, the error for v, p, and c is second-order for large Δt (shaded grey), but then deviates as Δt decreases. The error for u is not shown because it is indistinguishable from that for v. The order of accuracy for velocity decreases to approximately 1.17, while that for c tends to roughly 1.5. The decrease in temporal accuracy is observed for $\kappa = 0.001$ as well, and persists when osmotic pressure effects are removed by setting $A = 0$. This leaves the coupling between v_m and p_m as the likely culprit.

3.2. The improved method

We hypothesize that the deviation from second-order temporal accuracy of the base method occurs due to the viscous term $\nabla_d^2 \left(\mathbf{u}_P^{n+1} - \mathbf{u}_P^*\right)$ that was neglected in Eq. (18). This hypothesis is motivated by the projection method of Kim and Moin [47], which neglects p^n when computing $\mathbf{u}^*$. In that case, several studies [4,5,47] have shown that neglecting the viscous term in Eq. (18) generates errors in the pressure field, particularly near the domain boundaries. These errors can be mitigated by either using p^n when computing $\mathbf{u}^*$, as in Bell et al. [3], or by including the viscous term in Eq. (18), as in Kim and Moin [47].

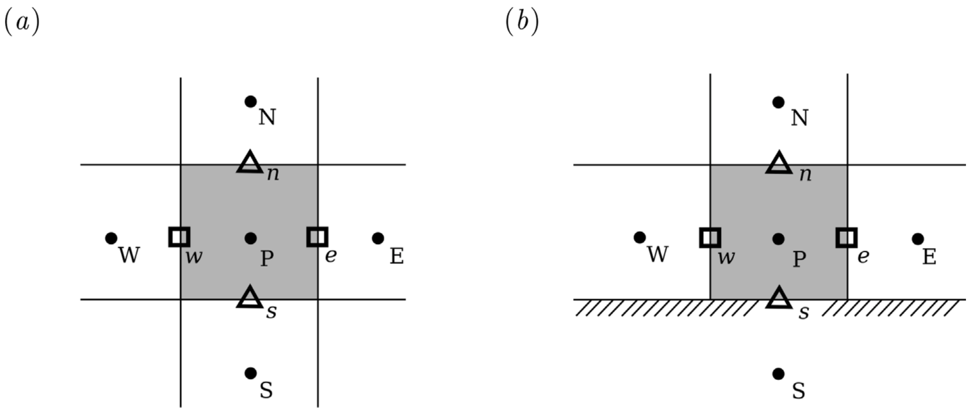

Fig. 4. Enforcing mass conservation on a pressure cell for (*a*) an internal cell and (*b*) a boundary cell.

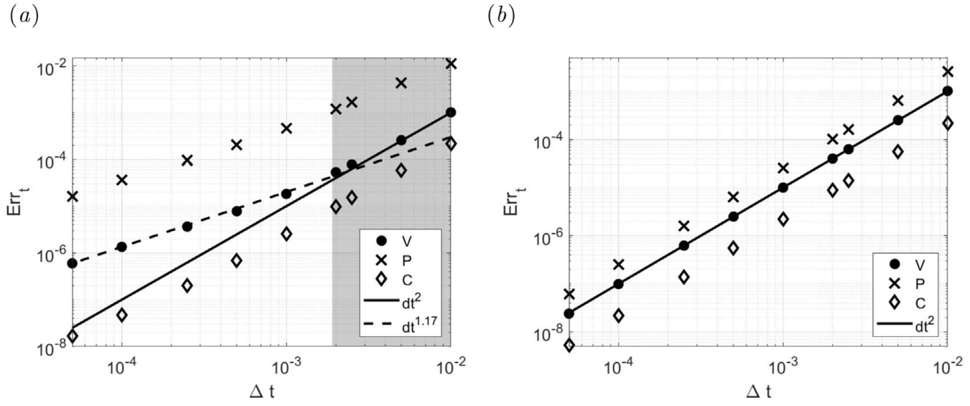

Fig. 5. Temporal accuracy of the (*a*) base method and (*b*) improved method when $K = 0.01$.

To explore our hypothesis, we include the viscous term by defining a new auxiliary variable $\hat{\phi}$ such that

$$p^{n+1} - p^n = \hat{\phi} - \alpha\mu\nabla^2\hat{\phi}. \tag{30}$$

It can be shown that $\mathbf{u}_p^{n+1}$ and $\mathbf{u}_p^*$ are then related by

$$\mathbf{u}_p^{n+1} = \mathbf{u}_p^* - \alpha\nabla_d\hat{\phi}_p, \tag{31}$$

where $\hat{\phi}$ satisfies the same Poisson Eq. (22) as ϕ. In summary, our improved method uses p^n when computing $\mathbf{u}^*$, as in Bell et al. [3], but uses the definition of $\hat{\phi}$ similar to Kim and Moin [47]. We apply Dirichlet conditions as in Bell et al. [3], by applying

$$\mathbf{u}^* = \mathbf{u}_b, \quad \mathbf{n}\cdot\boldsymbol{\nabla}\hat{\phi} = 0. \tag{32}$$

Note that this differs from the method of Kim and Moin [47]. Repeating our derivation of the membrane condition, it can be shown that $\hat{\phi}$ must satisfy the condition

$$\frac{\hat{\phi}_p - \hat{\phi}_S}{dy} - \frac{\kappa}{\alpha}\left(\frac{3}{2}\hat{\phi}_P - \frac{1}{2}\hat{\phi}_N\right) + \kappa\mu\left(\frac{3}{2}\nabla_d^2\hat{\phi}_P - \frac{1}{2}\nabla_d^2\hat{\phi}_N\right) = 0, \tag{33}$$

where the subscripts denote the node location labelled in Fig. 4(*b*). A detailed derivation is provided in Appendix C. Though initial versions of our code used condition (33), subsequent versions used the Poisson Eq. (22) to express the condition more simply as

$$\frac{\hat{\phi}_p - \hat{\phi}_S}{dy} - \frac{\kappa}{\alpha}\left(\frac{3}{2}\hat{\phi}_P - \frac{1}{2}\hat{\phi}_N\right) = -\frac{\kappa\mu}{\alpha}\left(\frac{3}{2}\boldsymbol{\nabla}_d\cdot\mathbf{u}_P^* - \frac{1}{2}\boldsymbol{\nabla}_d\cdot\mathbf{u}_N^*\right), \tag{34}$$

which is equivalent to the Robin condition $\partial\hat{\phi}/\partial y - (\kappa/\alpha)\hat{\phi} = -(\kappa\mu/\alpha)\boldsymbol{\nabla}_d\cdot\mathbf{u}^*$.

Repeating the benchmarking procedure outlined in Section 3.1, we find that the spatial and temporal accuracy of the improved method are both second-order. The temporal results for $\kappa = 0.01$ are shown in Fig. 5(*b*). This confirms our hypothesis that neglecting the viscous terms in Eq. (18) lowers the temporal accuracy of the base method.

4. Application of outlet conditions

To explore the application of outlet conditions, we consider a bench-scale RO system of height $h = 1$ mm and length $L = 10$ cm without a feed spacer. We set the inlet feed concentration to $C_{in} = 1$ g/l of NaCl, and the outlet pressure to $P_{out} = 20$ bar. We consider the typical membrane permeance $\kappa = 2.5{\times}10^{-12}$ ms^{-1}Pa^{-1} [7]. The inlet velocity is varied to consider Reynolds numbers between $50 \le \mathrm{Re} \le 500$, for which the system converges to a steady-state. To allow flow perturbations to exit the domain, we apply the convective conditions (6). Though not always discussed in prior literature, these are often discretized explicitly in time as

$$\frac{f^{n+1} - f^n}{\Delta t} + U_{in}\frac{\partial f^n}{\partial x} = 0.$$

This allows the outlet conditions for $\mathbf{u}^{n+1}$ to be expressed as equivalent Dirichlet conditions. The resulting outlet profile for u^{n+1}, however, must be rescaled to ensure mass conservation. This approach is not possible for RO, because the permeate mass flow is not known a-priori. We consequently use the procedure of Lou et al. [41] that discretizes the outlet condition implicitly as

$$\frac{f^{n+1} - f^n}{\Delta t} + U_{in}\frac{\partial f^{n+1}}{\partial x} = 0. \tag{35}$$

This produces a Robin condition that is applied to $\mathbf{u}^*$ as in Eq. (15).

To fix the outlet pressure using the base method, we apply the following outlet condition to ϕ,

$$\phi\Big|_{x=L} = P_{out} - p^n\Big|_{x=L}, \tag{36}$$

which follows from Eq. (19). Using the nodes labelled in Fig. 6(a), this is discretized as

$$\phi\Big|_{x=L} = \frac{\phi_W + \phi_E}{2}, \quad p^n\Big|_{x=L} = \frac{3}{2}p^n_W - \frac{1}{2}p^n_{WW}.$$

Note again that we must extrapolate $p^n\Big|_{x=L}$. When using the improved method, we fix the outlet pressure using the following outlet condition for $\hat{\phi}$,

$$\left[\hat{\phi} - \alpha\mu\nabla_d^2\hat{\phi}\right]_{x=L} = P_{out} - p^n\Big|_{x=L}, \tag{37}$$

which follows from Eq. (30). Here, $\nabla_d^2\hat{\phi}$ must be extrapolated from the interior of the domain. In a similar fashion to Eq. (34), we use the Poisson Eq. (22) to express the outlet condition as

$$\hat{\phi}\Big|_{x=L} = P_{out} - p^n\Big|_{x=L} + \mu\left(\frac{3}{2}\boldsymbol{\nabla}_d\cdot\mathbf{u}^*_W - \frac{1}{2}\boldsymbol{\nabla}_d\cdot\mathbf{u}^*_{WW}\right). \tag{38}$$

The combination of outlet conditions (35)–(36) was previously studied by Lou et al. [41], who showed they conserve mass to machine precision while allowing flow structures to exit the domain. As reported by Lou et al. [41], we also found that flow perturbations exit the domain more cleanly when we discretize the advection terms in Eq. (13) using a “minmod” TVD scheme. We refer to [41] and [55] for details.

To explore the performance of outlet conditions (33)–(35), we first perform a series of mesh-independence studies. For that purpose, we set the number of cells in the y-direction to $N_y = 200$ and vary the number of cells in the x-direction between $32 \le N_x \le 768$. For each N_x, we run the simulation to steady state and compute the spatial error

$$E_{N_x} = \frac{\|f_{N_x} - f_{768}\|_\infty}{\|f_{768}\|_\infty}, \tag{39}$$

where f_{N_x} is the solution using N_x cells. The spatial error in the y-direction is similarly calculated by setting $N_x = 400$ and varying N_y between $32 \le N_y \le 512$. We find that mass is well conserved in all cases, such that $\boldsymbol{\nabla}_d \cdot \mathbf{u}$ was on the order of 10^{-12}. We find that the error is second-order for all variables except for c, which shows roughly first-order accuracy. Similar results were obtained for the error with N_y. Further investigation showed that the errors were maximized near the channel inlet and outlet. Fig. 6(b) shows that if we exclude 1% of the domain length at the inlet and outlet in the computation of E_{N_x}, we recover second-order accuracy for all variables. Though not shown here for brevity, we also explored the impact of outlet conditions on spatial–temporal accuracy by repeating the benchmarking procedure outlined in Section 3.1. For that purpose, the exact velocity $\mathbf{u_e}$ was applied to $\mathbf{u}^*$ on all boundaries during prediction; however, the pressure was fixed to p_e on the right boundary ($x = 2\pi$) using Eq. (38). For consistency, we also discretized all advection terms using the minmod TVD scheme. The results showed second-order spatial–temporal accuracy.

The sensitivity of RO systems to inlet and outlet conditions is relatively well documented [56–58]. As suggested by Tilton et al. [56], we explored the application of “permeability buffers” in which the membrane permeance is smoothly ramped down to zero at the inlet and outlet. We found this method recovered second-order accuracy. However, given that this approach consumes more than 1% of the system length at the inlet and outlet, we decided they were not warranted. In addition to the tests reported here, further tests found that the outlet conditions performed well in the presence of a feed spacer, as demonstrated in Appendix E.

5. Reverse osmosis with a feed spacer

We now use our numerical method to explore transition to vortex shedding in a 2D plate-and-frame RO system with a single spacer filament. We consider a system of height $h = 1$ mm and length $L = 12$ cm. We place a filament of diameter $D_c = 0.5$ mm ($h/2$) on the channel centre-line ($y_c = h/2$) a distance of 5 diameters from the inlet ($x_c = 5D_c$). We set the inlet concentration, membrane permeance, and operating pressure to $C_{in} = 35$ g/l NaCl, $\kappa = 2.5 \times 10^{-12}$ ms^{-1}Pa^{-1}, and $P_{out} = 40$ bar, which is typical of seawater RO. We vary the Reynolds number $Re = \rho U_{in} h/\mu$ between $50 \le Re \le 350$ to capture both steady and unsteady laminar flow regimes. For comparison, simulations are repeated both with and without spacers. Transition to vortex shedding occurred at $Re = 170 \pm 2$. This compares well with the critical Reynold numbers predicted by a theoretical study of flow over a cylinder in a channel with impermeable walls [42].

Fig. 7 shows steady-state results for the sub-critical Reynolds number $Re = 50$ ($U_{in} = 4.6 \times 10^{-2}$ m/s). The streamlines in panel (a) show a pair of counter-rotating vortices in the cylinder wake. Panel (b) shows the concentration field near the membrane, $y/h \le 0.1$. The concentration is equal to the inlet value C_{in} everywhere except in a thin boundary layer near the membrane. The dashed white line shows the concentration boundary layer thickness, $\delta(x)$, at which $c = 1.002C_{in}$. The filament redirects and accelerates low concentration bulk fluid towards the membrane surface, compressing the boundary layer beneath the filament. Panel (c) shows the downstream variation of the concentration on the membrane, $C_m(x)$, normalized with C_{in}. Panel (d) shows the local permeate flux $v_m(x)$, normalized with U_{in}. We define v_m as positive when permeate leaves the channel. The dashed lines show the corresponding results without a spacer. We see that the spacer has a strong influence one diameter upstream and 6–7 diameters downstream. C_m has a local minimum beneath the filament and then slowly tends downstream to the result observed without the spacer. Note that spatial variations in the pressure field p were found to be less than 0.01% of P_{out}. The variations in $v_m(x)$ in Fig. 7(d) consequently arise due to osmotic pressure effects.

Fig. 8 shows results for the super-critical case Re = 300 ($U_{in} = 0.276$ m/s). Panels (a) and (b) show snapshots of the instantaneous streamlines and vorticity $\omega = \partial v/\partial x - \partial u/\partial v$, respectively. Instability causes periodic shedding of vortices in the filament wake. The vortices then dissipate as they are advected downstream. Though ω varies between roughly $-33000 \le \omega \le 33000$ s^{-1}, we set the limits of the colour scale in Fig. 8(b) to $-2000 \le \omega \le 2000$ s^{-1} to better highlight these vortical structures. The streamlines in panel (a) also show the appearance of vortical structures on the membrane and outer plate. These structures periodically appear near $x/h = 3.5$, travel downstream, and dissipate near $x/h = 4.5$. Panel (c) shows a snapshot of the concentration field near the membrane, $y/h \le 0.1$. Panels (d) and (e) show the corresponding membrane concentration $C_m(x)/C_{in}$ and permeate flux $v_m(x)/U_{in}$, respectively. As observed for $Re = 50$, the filament redirects low concentration fluid towards the membrane, decreasing polarization below the spacer. Downstream, however, we observe localized solute accumulation on the membrane near $x/h = 3.5$. This occurs in the region over which the vortical structure travels along the membrane. Fig. 9 shows four sequential snapshots of the concentration field and streamlines in the region of solute accumulation. These suggest that solute accumulation occurs due to flow reversal beneath the travelling vortex, which advects solutes upstream. The mechanism can be explained using the points labelled $a - d$ in the snapshot labelled t_3. As feed flows downstream from point a to point b, its concentration increases as solvent passes through the membrane. Similarly, flow moving upstream from point c to point d also increases in concentration. The concentration consequently tends to accumulate near the leading edge of the vortex.

Fig. 8(f) shows the downstream variation of the membrane feed surface pressure p_m for $Re = 300$. Results are shown both with (solid line) and without (dashed line) the spacer filament. Overall, we see that for a single filament in a short system, downstream pressure variations are small. This lends support to CFD studies in the membrane filtration

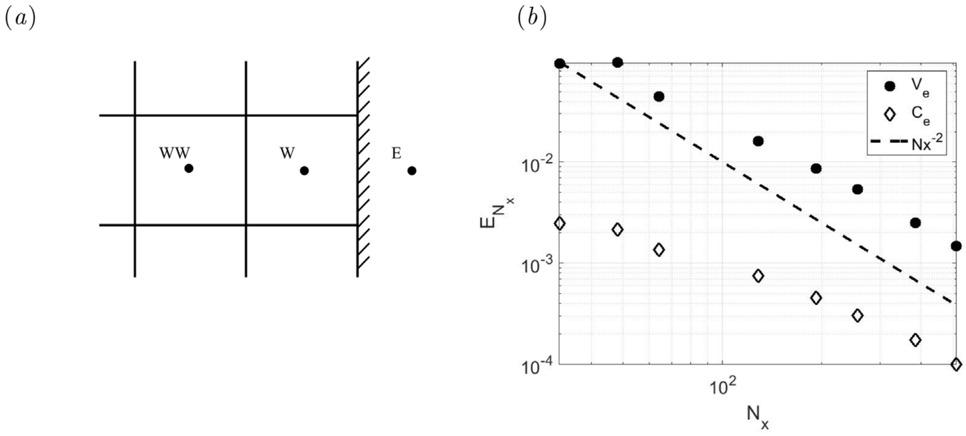

Fig. 6. (*a*) Application of outlet condition (36) (*b*) Grid independence study excluding 1% of domain at inlet and outlet.

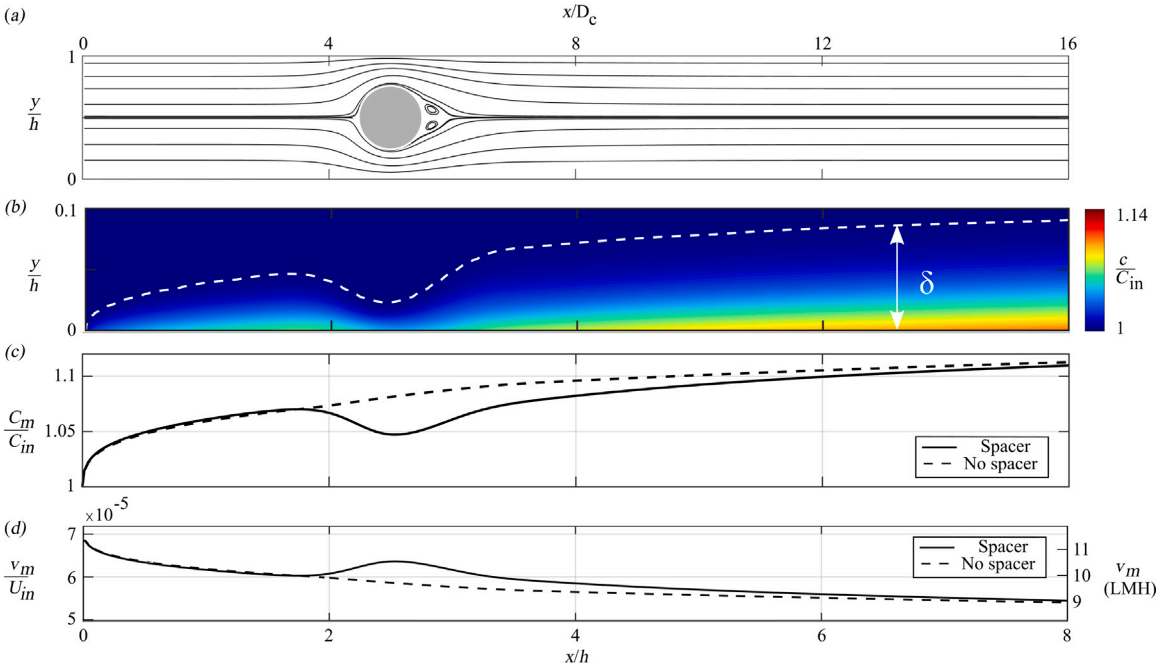

Fig. 7. Results when $Re = 50$. For convenience, we present the position as both x/h and x/D_c. (*a*) Streamlines. (*b*) Concentration field near membrane, $y/h \leq 0.1$. The dashed white line shows the concentration boundary layer. (*c*) Concentration on the membrane with spacer (solid line) and without (dashed line). (*d*) Permeate flux v_m/U_{in} with spacer (solid line) and without (dashed line).

community that approximate the membrane condition (1) as

$$v_m = \kappa\left[P_{out} - p_p - \Pi\right],$$

to remove the coupling of v_m to the local pressure field. For realistic RO systems with tightly packed filaments, and a system length near 1 metre, this assumption remains to be explored.

Fig. 10 shows the variation of the average permeate flux j_v and maximum concentration C_{max} with Reynolds number, where

$$j_v = \frac{1}{5h}\int_0^{5h} v|_{y=0}dx.$$

These are computed for the region $0 \leq x/h \leq 5$ to focus on the near-spacer region. Results are shown with the spacer (solid lines) and without (dashed lines). For the parameters considered in this study, we find that the average flux increases monotonically with Reynolds number, and the filament increases permeate production by roughly 2%. When no spacer is present, the maximum concentration decreases monotonically with Reynolds number. When the spacer is present, however, C_{max} initially decreases for sub-critical Reynolds numbers, and then increases after transition to vortex shedding. Similar behaviour is seen in simulations of spacer filaments in direct contact membrane distillation. In that case, Lou et al. [41] suggest there might be a trade off between increasing permeate production and increased risk of salt precipitation.

6. Conclusions

We showed that the temporal accuracy of the popular projection method of Bell et al. [3] drops to first order when simulating reverse osmosis systems. The drop in accuracy occurs due to the coupling between the velocity and the pressure fields in the membrane boundary conditions, which causes errors in the pressure field to pollute the velocity field. We showed, however, that second-order accuracy can be recovered using a modified intermediate variable $\hat{\phi}$, as shown in Eq. (30). In addition to the unique coupling between the velocity and pressure fields, RO systems present further challenges at the inlet and outlet. To that end, we showed the improved projection method can accommodate outlet conditions that fix the operating pressure while

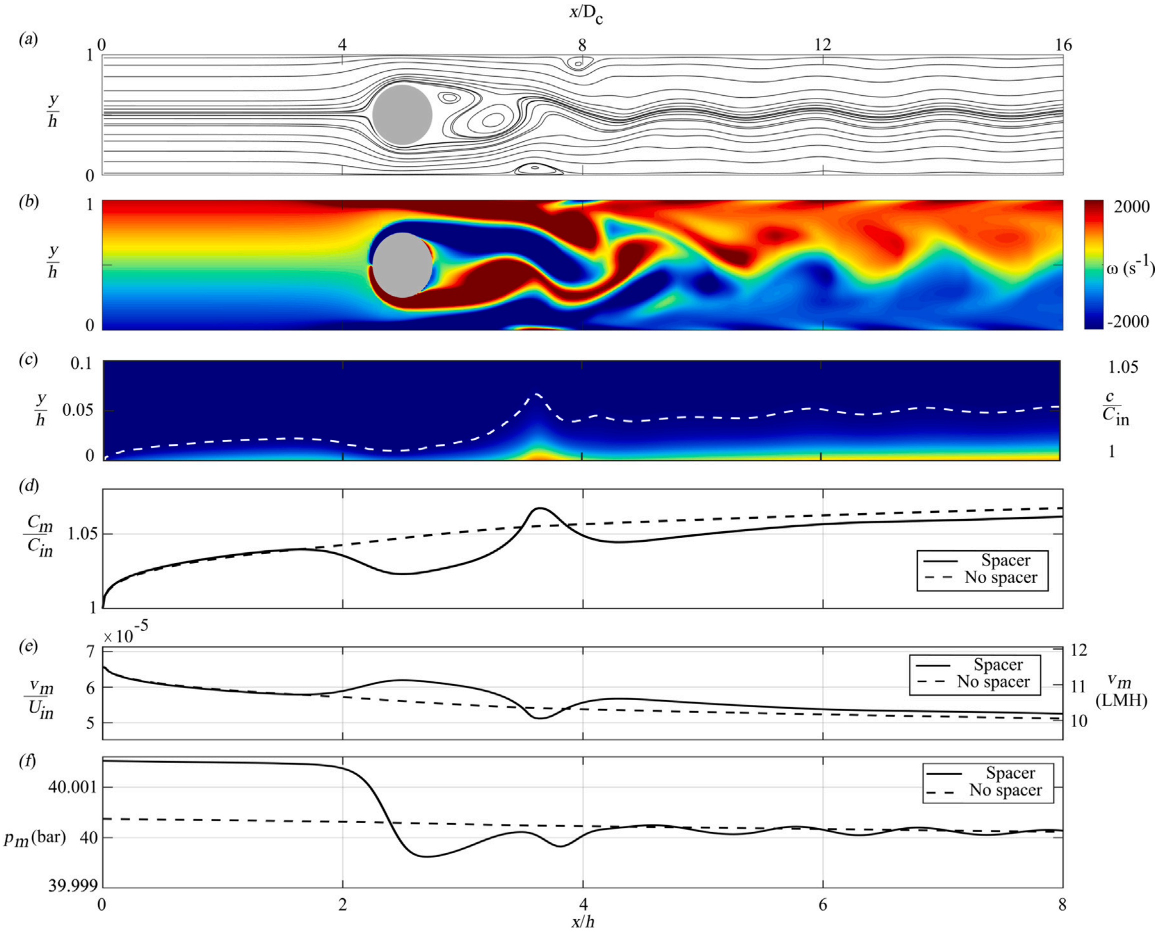

Fig. 8. Results when $Re = 300$. (*a*) Instantaneous streamlines. (*b*) Instantaneous vorticity. (*c*) Instantaneous concentration field near membrane. The dashed white line shows the concentration boundary layer. (*d*) Concentration on the membrane with spacer (solid line) and without (dashed line). (*e*) Permeate flux v_m/U_{in} with spacer (solid line) and without (dashed line). (*f*) Membrane pressure p_m with spacer (solid line) and without (dashed line).

allowing flow perturbations to exit the domain, all while satisfying conservation of mass.

To test our methods, we coupled the improved projection method with the immersed boundary method of Lou et al. [41] to simulate the impact of vortex shedding on concentration polarization in a plate-and-frame RO system with a single spacer filament. Within the limits of the current study, we showed that in steady flow regimes, the spacer filament reduces the concentration on the membrane and increases the permeate production in comparison to when no spacer is present. In the super-critical regime, we found that the spacer increases permeate production, but generates a region of preferential solute accumulation that could lead to mineral scaling. Though beyond the scope of the current study, we are now performing a parametric study of 2D filament arrays to explore the impact of vortex shedding for a broad range of operating conditions and membrane permeances. We are also expanding our methods to 3D and performing parallel experiments for comparison. Finally, we note that the current study focuses on projection methods because they are popular for simulating unsteady, incompressible flows. Future work may want to similarly investigate the impact of Darcy-type boundary conditions on the spatial–temporal accuracy of SIMPLE-type schemes [51,59] or the more recent methods developed by Griffith and colleagues [60–62].

This work was generously funded by a National Science Foundation Career Award (1752531) and the Embassy of France Thomas Jefferson Fund. The authors thank Dr. John Farnsworth (University of Colorado, Boulder) and Dr. Denis Martinand (University of Aix-Marseille) for helping interpret vortical flow structures. We also thank Dr. Tony Saad and Mokbel Karam (University of Utah) for helping interpret the behaviour of the base projection method. Finally, we thank Drs. Paul Martin and Greg Fasshauer (Colorado School of Mines) for helping derive outlet conditions (36)–(38).

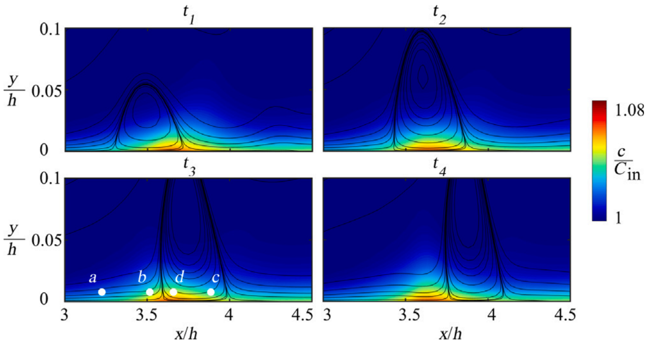

Fig. 9. Snapshots of the concentration field super-imposed with streamlines in the region of concentration accumulation $3 \leq x/h \leq 4.5$, $0 \leq y/h \leq 0.1$. Snapshots are taken at equispaced times $t_1 < t_2 < t_3 < t_4$, where $t_2 - t_1 = 4 \times 10^{-3}$ s. The points labelled $a-d$ are discussed in the text.

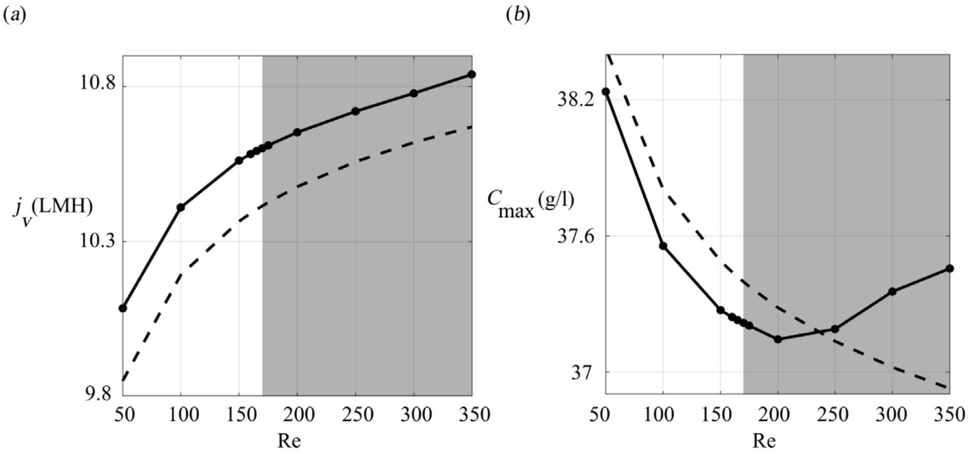

Fig. 10. (*a*) Average flux and (*b*) maximum membrane concentration vs Reynolds number. The shaded region shows super-critical Reynolds numbers. Dashed lines show results without spacers and dotted lines show results with spacers.

CRediT authorship contribution statement

Jacob Johnston: Software, Validation, Formal analysis, Writing – original draft. **Jincheng Lou:** Software, Validation, Formal analysis. **Nils Tilton:** Conceptualization, Software, Formal analysis, Resources, Supervision, Funding acquisition, Writing – review & editing.

Declaration of competing interest

One or more of the authors of this paper have disclosed potential or pertinent conflicts of interest, which may include receipt of payment, either direct or indirect, institutional support, or association with an entity in the biomedical field which may be perceived to have potential conflict of interest with this work. For full disclosure statements refer to https://doi.org/10.1016/j.compfluid.2021.105189.Nils Tilton reports financial support was provided by National science Foundation. Nils Tilton reports financial support was provided by Embassy of France Thomas Jefferson Fund.

Appendix A. Thermophysical properties

The dynamic viscosity $\mu(T,c)$, density $\rho(T,c)$, and mass diffusivity $\mathcal{D}(c)$ of the NaCl solution are evaluated using the relationships,

$$\mu(T,c) = A_v(T)c^4 + B_v(T)c^3 + C_v(T)c^2 + D_v(T)c + E_v(T). \tag{A.1}$$

$$A_v = -1.63\times 10^{-14}, \quad B_v = 1.57\times 10^{-11}, \quad C_v = 1.04\times 10^{-9},$$

$$D_v = 1.35\times 10^{-6}, \quad E_v = 8.90\times 10^{-4}.$$

$$\rho(T,c) = A_\rho c^3 + B_\rho c^2 + C_\rho c + D_\rho. \tag{A.2}$$

$$A_\rho = 1.56\times 10^{-7}, \quad B_\rho = -1.92\times 10^{-4}, \quad C_\rho = 0.68, \quad D_\rho = 997.$$

$$\mathcal{D}(c) = 10^{-09} \times \frac{A_d + \frac{1000}{\mathcal{M}} B_d c}{1 + \frac{1000}{\mathcal{M}} C_d c + D_d(\frac{1000c}{\mathcal{M}})^2}. \tag{A.3}$$

$$A_d = 1.418, \quad B_d = 1.159{\times}10^{-01}, \quad C_d = 8.50{\times}10^{-02}, \quad D_d = 1.514{\times}10^{-05},$$

where $\mathcal{M} = 58.44$ g/mol is the molecular weight of NaCl. These relationships assume $T_{in} = 25$ °C. The correlations for $\mu(T,c)$ and $\rho(T,c)$ were derived using the OLI Stream Analyzer database (OLI Systems, Morris Plains, NJ). We obtained the correlation for $\mathcal{D}(c)$ from the Ref. [9].

Appendix B. Discretization on non-uniform grids

To demonstrate our discretization of the governing equations (2)–(4), consider the x-component of the Navier–Stokes Eqs. (2) written in control volume form as

$$\int_{CV} \rho \frac{\partial u}{\partial x} dV + \int_S \rho(\mathbf{u}\cdot\mathbf{n}) dA = -\int_S p(\mathbf{i}\cdot\hat{n}) ds + \int_S \mu \nabla u \cdot \mathbf{n} dA, \tag{B.1}$$

where $\mathbf{i}$ is the unit vector in the x- direction, $\mathbf{n}$ is the unit normal vector pointing away from the control surface S of the control volume CV sketched in Fig. B.11(*a*). We approximate the unsteady and pressure terms as

$$\int_{CV} \rho \frac{\partial u}{\partial t} dV = \rho \frac{\partial u_p}{\partial t} dx dy, \qquad \int_S p(\mathbf{i}\cdot\mathbf{n}) = dy(p_e - p_w), \tag{B.2}$$

where dx and dy are labelled in Fig. B.11(*a*). The advection term is discretized using the “minmod” TVD scheme [55], as detailed in Lou et al. [41]. Finally, we approximate the viscous terms using Fig. B.11(*b*) as,

$$\int_S \mu(\nabla u\cdot\mathbf{n}) dA \approx \mu \frac{\partial u_e}{\partial x} dy + \mu \frac{\partial u_n}{\partial y} dx - \mu \frac{\partial u_w}{\partial x} dy - \mu \frac{\partial u_s}{\partial y} dx, \tag{B.3}$$

where the gradients are approximated using centred differences, such as

$$\frac{\partial u_e}{\partial x} \approx \frac{u_E - u_P}{x_E - x_P}. \tag{B.4}$$

We similarly discretize the y-momentum equation using the control volume sketched in Fig. B.11(*b*). We then find that Eq. (20) is expressed in discrete form as

$$u_P^{n+1} = u_P^* - \alpha\left(\frac{\phi_e - \phi_w}{dx}\right), \qquad v_P^{n+1} = v_P^* - \alpha\left(\frac{\phi_n - \phi_s}{dy}\right), \tag{B.5}$$

where the subscripts denote the locations labelled in Fig. B.11(*a*) and (*b*). Using the pressure cell in Fig. B.11(*c*), we discretize the conservation of mass equation as

$$\frac{u_e^{n+1} - u_w^{n+1}}{dx} + \frac{v_n^{n+1} - v_s^{n+1}}{dy} = 0. \tag{B.6}$$

Substituting relations (B.5) into the above, we find the discrete Poisson equation

$$\frac{1}{dx}\left(\frac{\phi_E - \phi_P}{x_E - x_P} - \frac{\phi_P - \phi_W}{x_P - x_W}\right) + \frac{1}{dy}\left(\frac{\phi_N - \phi_P}{y_N - y_P} - \frac{\phi_P - \phi_S}{y_P - y_S}\right)$$
$$= \frac{1}{\alpha}\left(\frac{u_e^* - u_w^*}{dx} + \frac{v_n^* - v_s^*}{dy}\right). \tag{B.7}$$

For the base projection method, we apply the discrete Poisson equation using ghost nodes on boundary cells, such as that sketched in

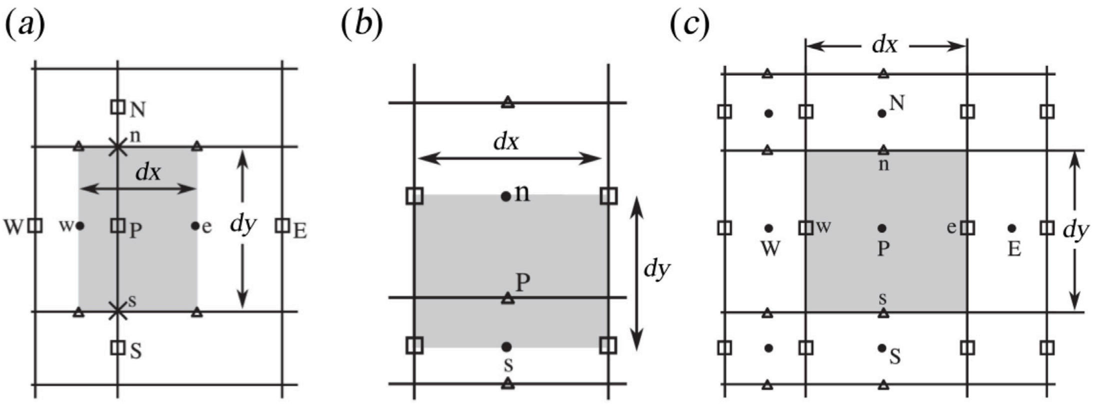

Fig. B.11. The staggered grid. The fields u, v, and p are stored at the locations marked as squares, triangles, and solid dots, respectively. (a) The control volume (shaded grey) used to discretize momentum in the x-direction. (b) The control volume (shaded grey) used to discretize momentum in the y-direction.(c) A pressure cell (shaded grey).

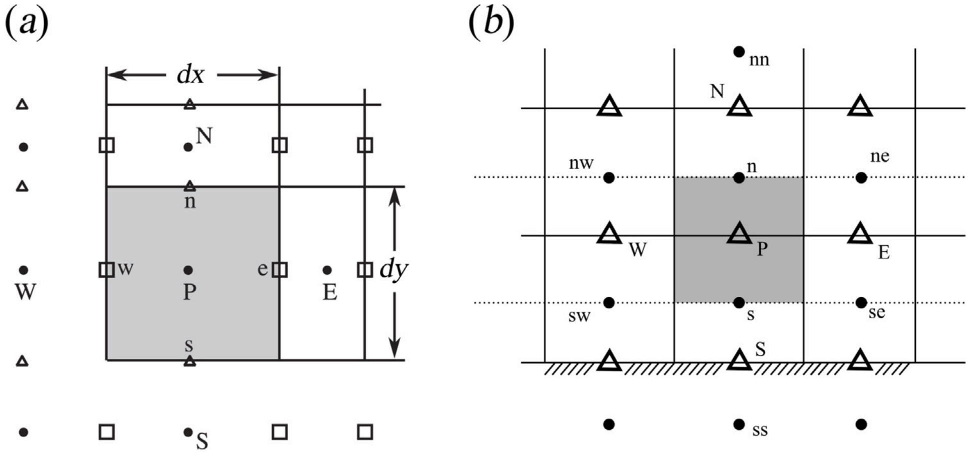

Fig. C.12. (a) A corner pressure cell (shaded grey) with ghost nodes. (b) Membrane Boundary Condition Requires Additional Modification.

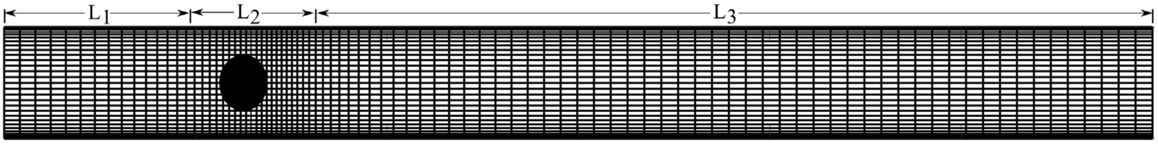

Fig. D.13. Demonstration of grid using $N_x = 90$, $N_y = 30$.

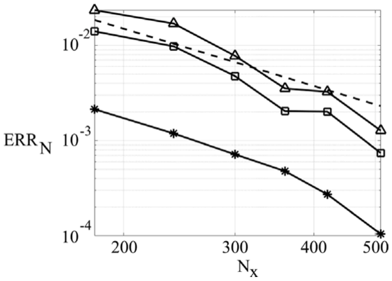

Fig. D.14. Variations of spatial error with N_x for u (squares), v (triangles), and c (asterisks). The dashed line shows $1/N^2$.

Fig. C.12(a). The Neumann conditions for the two boundaries of this corner cell are then applied as

$$\frac{\phi_P - \phi_W}{dx} = 0, \quad \frac{\phi_P - \phi_S}{dy} = 0. \tag{B.8}$$

Appendix C. Membrane boundary conditions

To demonstrate the derivation of the membrane conditions for ϕ, consider a grid of uniform spacing dx and dy. Subtracting the discretized Eq. (17) from (14) it is straightforward to show that

$$p_P^{n+1} = p_P^n + \hat{\phi}_P - \frac{2\mu\Delta t}{3\rho}\nabla_d^2\hat{\phi}_P, \tag{C.1}$$

where ∇_d^2 is the discrete Laplacian defined Eq. (12).

To derive the membrane condition for $\hat{\phi}$, we first discretize the membrane conditions for v^{n+1} and v^* as

$$v_S^{n+1} = -K(\lambda p_s^{n+1} + Bp_n^{n+1}) \tag{C.2}$$

$$v_S^* = -K(\lambda p_s^n + Bp_n^n) \tag{C.3}$$

where λ and B are coefficients used for extrapolation based off of location of the nodes labelled in Fig. C.12(b). For uniform grids $\lambda = 3/2$,

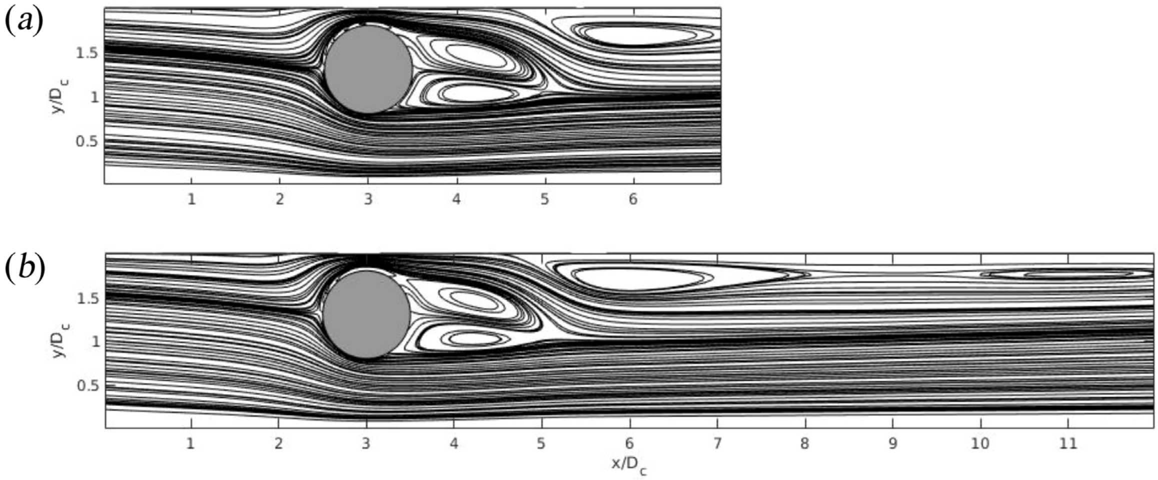

Fig. E.15. Comparison of two simulations of a channel flow with $Re = 320$ and a blockage ratio $\beta = 0.5$ using a short (a) and long (b) domain.

$B = -1/2$. Subtracting (C.3) from (C.2)

$$v_S^{n+1} - v_S^* = -K\left[\lambda(p_s^{n+1} - p_s^n) + B(p_n^{n+1} - p_n^n)\right],$$

and substituting

$$v_S^{n+1} - v_S^* = -\alpha\frac{\hat{\phi}_s - \hat{\phi}_{ss}}{dy},$$

we find that

$$-\alpha\frac{\hat{\phi}_s - \hat{\phi}_{ss}}{dy} = -K\left[\lambda(p_s^{n+1} - p_s^n) + B(p_n^{n+1} - p_n^n)\right]. \tag{C.4}$$

Finally, we can express $p^{n+1} - p^n$ in terms of $\hat{\phi}$ using Eq. (C.1).

$$-\frac{\alpha}{K}\frac{\hat{\phi}_s - \hat{\phi}_{ss}}{dy} = -\lambda\hat{\phi}_s - B\hat{\phi}_n + \tag{C.5}$$

$$\alpha\lambda\mu\left[\frac{\hat{\phi}_{sw} - 2\hat{\phi}_s + \hat{\phi}_{se}}{dx^2} + \frac{\hat{\phi}_{ss} - 2\hat{\phi}_s + \hat{\phi}_n}{dy^2}\right]$$

$$+\ \alpha B\mu\left[\frac{\hat{\phi}_{nw} - 2\hat{\phi}_n + \hat{\phi}_{ne}}{dx^2} + \frac{\hat{\phi}_s - 2\hat{\phi}_n + \hat{\phi}_{nn}}{dy^2}\right].$$

Once again, we can use Eq. (22) to replace the Laplacian term. The boundary condition for ϕ using the base projection method is the same as in Eq. (C.5) except the viscous terms are set to zero

$$-\frac{\alpha}{K}\frac{\hat{\phi}_s - \hat{\phi}_{ss}}{dy} = -\lambda\hat{\phi}_s - B\hat{\phi}_n. \tag{C.6}$$

Repeating this derivation on a non-uniform grid, one can show that the discrete Laplace operators on the right hand side of Eq. (C.5) are replaced with the Laplace operator demonstrated in Eq. (B.7).

Appendix D. Grid independence studies

Our simulations of RO systems concentrate cells near the membrane and outer wall by setting the y-coordinates of the horizontal faces to

$$y_i = (h/2)(1 + \cos(\pi i/N_y)), \quad i = 0, 1, \ldots, N_y, \tag{D.1}$$

which are the Gauss–Lobatto–Chebyshev points mapped to interval $y \in [0, h]$. Simulations without spacers use N_x equispaced cells in the x-direction. Simulations with spacers refine the grid near the cylinder by decomposing the x-direction into three sections, as demonstrated in Fig. D.13. The core section, L_2, begins one cylinder diameter upstream of the cylinder centre and ends two cylinder diameters downstream of the cylinder centre. This section has N_2 equispaced cells in the x-direction. For the purposes of this study $N_2 = N_y$. For the other sections, N_1 and N_3 are determined such that $N_1 + N_2 + N_3 = N_x$ and that the cells in the first and third sections each share the same cell size in the x-direction. The sharp transition in cell sizes is then smoothed by looping through each point and setting its x value to be the average of its two neighbours in the x-direction. This process is repeated 20 times for the grid in Fig. D.13.

To demonstrate our mesh independence studies, we consider here the simulation shown in Fig. 7, for which the flow fields can be integrated to steady state. We fix the ratio $N_x/N_y = 3$ and vary N_x and N_y between $180 \le N_x \le 600$ and $60 \le N_y \le 200$, respectively. Simulations were run to steady-state, after which the spatial error, ERR_N, was evaluated using the result at $(N_x, N_y) = (600, 200)$ as the exact solution. Fig. D.14 shows the error is below 1% when $N_x > 300$.

Appendix E. Outlet study with feed spacer

To gauge how well the outlet conditions perform when vortical flow structures are present, we considered flow over a cylinder in a planar channel flow. Fig. E.15 shows two simulations performed for $Re = 320$ and blockage ratio $\beta = 0.5$ with the cylinder located closer to the upper wall. Zovatto and Pedrizzetti [63] have shown that the asymmetry stabilizes vortex shedding and produces elongated vortical structures behind the cylinder and along the upper wall. The cylinder is placed three diameters downstream of the inlet. Fig. E.15(a) shows a simulation using $L_x = 3.5$ mm such that the outlet cuts through the vortex. Panel (b) shows the simulation using $L_x = 6$ mm. Comparison of the streamlines shows minimal upstream influence of the outlet conditions.

References

[1] Ghaffour N, Missimer TM, Amy G. Technical review and evaluation of the economics of water desalination: Current and future challenges for better water supply sustainability. Desalination 2013;309:197–207.

[2] Wintgens T, Melin T, Schafer A, Khan S, Muston M, Bixio D, et al. The role of membrane processes in municipal wastewater reclamation and reuse. Desalination 2005;178:1–11.

[3] Bell J, Colella P, Glaz H. A second-order projection method for the incompressible Navier-Stokes equations. J Comput Phys 1988;85:257–83.

[4] Brown D, Cortez R, Minion M. Accurate projection methods for the incompressible Navier-Stokes equations. J Comput Phys 2001;168:464–99.

[5] Guy R, Fogelson A. Stability of approximate projection methods on cell-centered grids. J Comput Phys 2005;203:517–38.

[6] Guermond J, Minev P, Shen J. An overview of projection methods for incompressible flows. Comput Methods Appl Mech Engrg 2006;195:6011–45.

[7] Wagner EMV, Sagle AC, Sharma MM, Freeman BD. Effect of crossflow testing conditions, including feed pH and continuous feed filtration, on commercial reverse osmosis membrane performance. J Membr Sci 2009;345(1–2):97–109. http://dx.doi.org/10.1016/j.memsci.2009.08.033.

[8] Bear J. Dynamics of fluids in porous media. Dover; 1972.

[9] Lyster E, Cohen Y. Numerical study of concentration polarization in a rectangular reverse osmosis membrane channel: Permeate flux variation and hydrodynamic end effects. J Membr Sci 2007;303:140–53.

[10] Matin A, Rahman F, Shafi H, S. Z. Scaling of reverse osmosis membranes used in water desalination: Phenomena, impact, and control; future directions. Desalination 2019;455:135–57.

[11] Xie M, Tang C, Gray S. Spacer-induced forward osmosis membrane integrity loss during gypsum scaling. Desalination 2016;392:85–90.

[12] Xu P, Bellona C, Drewes J. Fouling of nanofiltration and reverse osmosis membranes during municipal wastewater reclamation: Membrane autopsy results from pilot-scale investigations. J Membr Sci 2010;353:111–21.

[13] Coday B, Almaraz N, Cath T. Forward osmosis desalination of oil and gas wastewater: Impacts of membrane selection and operating conditions on process performance. J Membr Sci 2015;488:40–55.

[14] Lee S, Kim J, Lee C. Analysis of Caso4 scale formation mechanism in various nanofiltration modules. J Membr Sci 1999;163:63–74.

[15] Pervov A. Scale formation prognosis and cleaning procedure schedules in reverse osmosis systems operation. Desalination 1991;83:77–118.

[16] Gimmelshtein M, Semiat R. Investigation of flow next to membrane walls. J Membr Sci 2005;264:137–50.

[17] Thomas D, Hayes P, Mixon W, Sheppard J. Turbulence promoters for hyperfiltration with dynamic membranes. Environ Sci Technol 1970;4:1129–36.

[18] Subramani A, Kim S, Hoek E. Pressure, flow, and concentration profiles in open and spacer-filled membrane channels. J Membr Sci 2006;277(1–2):7–17. http://dx.doi.org/10.1016/j.memsci.2005.10.021.

[19] von der Schulenburg D, Vrouwenvelder J, Creber S, van Loosdrecht M, Johns M. Nuclear magnetic resonance microscopy studies of membrane fouling. J Membr Sci 2008;323:37–44.

[20] Ali S, Qamar A, Kerdi S, Phuntsho S, Vrouwenvelder J, Ghaffour N, et al. Energy efficient 3d printed column type feed spacers for membrane filtration. Water Res 2019;164.

[21] Haidari A, Heijman S, van der Meer W. Optimal design of spacers in reverse osmosis. Sep Purif Technol 2018;192:441–56.

[22] Keir G, Jegatheesan V. A review of computational fluid dynamics applications in pressure-driven membrane filtration. Rev Environ Sci Biotechnol 2014;13:183–201.

[23] Karode S. Laminar flow in channels with porous walls, revisited. J Membr Sci 2001;191:237–41.

[24] Wiley D, Fletcher D. Techniques for computational fluid dynamics modelling of flow in membrane channels. J Membr Sci 2003;211:127–37.

[25] Cao Z, Wiley D, Fane A. CFD simulations of net-type turbulence promoters in a narrow channel. J Membr Sci 2001;185:157–76.

[26] Karode S, Kumar A. Flow visualization through spacer filled channels by computational fluid dynamics I. Pressure drop and shear rate calculations for flat sheet geometry. J Membr Sci 2001;193:69–84.

[27] Li F, Meindersma W, de Haan A, Reith T. Optimization of commercial net spacers in spiral wound membrane modules. J Membr Sci 2002;208:289–302.

[28] Koutsou C, Yiantsios S, Karabelas A. Numerical simulation of the flow in a plane-channel containing a periodic array of cylindrical turbulence promoters. J Memb Sci 2004;231:81–90.

[29] Ahmad A, Lau K, Baker MA, Shukor SA. Integrated CFD simulation of concentration polarization in narrow membrane channel. Comput Chem Eng 2005;29:2087–95.

[30] Dendukuri D, Karode S, Kumar A. Flow visualization through spacer filled channels by computational fluid dynamics-II: improved feed spacer designs. J Memb Sci 2005;249:41–9.

[31] Koutsou CP, Yiantsios SG, Karabelas AJ. Direct numerical simulation of flow in spacer-filled channels: Effect of spacer geometrical characteristics. J Memb Sci 2007;291:53–69.

[32] Torras CT, Pallares J, Garcia-Valls R, Jaffrin MY. Numerical simulation of the flow in a rotating disk filtration module. Desalination 2009;235:122–38.

[33] Koutsou C, Yiantsios S, Karabelas A. A numerical and experimental study of mass transfer in spacer-filled channels: Effects of spacer geometrical characteristics and Schmidt number. J Memb Sci 2009;326:234–51.

[34] Ahmed S, Seraji MT, Jahedi J, Hashib M. CFD simulation of turbulence promoters in a tubular membrane channel. Desalination 2011;276(1–3):191–8. http://dx.doi.org/10.1016/j.desal.2011.03.045.

[35] Bucs S, Radu A, Lavric V, Vrouwenvelder J, Picioreanu C. Effect of different commercial feed spacers on biofouling of reverse osmosis membrane systems: A numerical study. Desalination 2014;343:26–37.

[36] Gurreri L, Tamburini A, Cipollina A, Micale G, Ciofalo M. CFD Prediction of concentration polairzation phenomena in spacer-filled channels for reverse electrodialysis. J Memb Sci 2014;468:133–48.

[37] Radu AI, van Steen MSH, Vrouwenvelder JS, van Loosdrecht MCM, Picioreanu C. Spacer geometry and particle deposition in spiral wound membrane feed channels. Water Res 2014;64:160–76.

[38] Picioreanu C, Vrouwenvelder J, van Loosdrecht M. Three-dimensional modeling of biofouling and fluid dynamics in feed spacer channels of membrane devices. J Membr Sci 2009;345:340–54.

[39] Radu A, Bergwerff L, van Loosdrecht M, Picioreanu C. A two-dimensional mechanistic model for scaling in spiral wound membrane systems. Chem Eng J 2014;241:77–91.

[40] Ling B, Battiato I. Rough or wiggly? Membrane topology and morphology for fouling control. J Fluid Mech 2019;862:753–80.

[41] Lou J, Johnston J, Tilton N. Application of projection and immersed boundary methods to simulating heat and mass transport in membrane distillation. Comput & Fluids 2020.

[42] Sahin M, Owens R. A numerical investigation of wall effects up to high blockage ratios on two-dimensional flow past a confined circular cylinder. Phys Fluids 2004;16:1305–20.

[43] Ponzio F, Tamburini A, Cipollina A, Micale G, Ciofalo M. Experimental and computational investigation of heat transfer in channels filled by woven spacers. Int J Heat Mass Transfer 2017;104:163–77.

[44] Li F, Meindersma W, de Haan A, Reith T. Experimental validation of cfd mass transfer simulations in flat channels with non-woven net spacers. J Membr Sci 2004;232:19–30.

[45] Ahmad A, Lau K. Impact of different spacer filaments geometries on 2d unsteady hydrodynamics and concentration polarization in spiral wound membrane channel. J Membr Sci 2006;286:77–92.

[46] Fimbres-Weihs G, Wiley D, Fletcher D. Unsteady flows with mass transfer in narrow zigzag spacer-filled channels: a numerical study. Ind Eng Chem Res 2006;45:6594–603.

[47] Kim J, Moin P. Application of a fractional-step method of incompressible Navier-Stokes equations. J Comput Phys 1985;59:308–23.

[48] Lou J, Vanneste J, DeCaluwe C, Cath T, Tilton N. Computational fluid dynamics simulations of polarization in direct contact membrane distillation. J Membr Sci 2019;591.

[49] Sani R, Shen J, Pironneau O, Gresho P. Pressure boundary condition for the time-dependent incompressible Navier-Stokes equations. Internat J Numer Methods Fluids 2006;50:673–82.

[50] Harvie CE, ller NM, Weare JH. The prediction of mineral solubilities in natural waters: The Na-K-Mg-Ca-H-Cl-SO4-OH-HCO3-CO3-CO2-H2O system to high ionic strengths at 25°C. Geochim Cosmochim Acta 1984;48(4):723–51. http://dx.doi.org/10.1016/0016-7037(84)90098-x.

[51] Ferziger J, Peric M. Computational methods for fluid dynamics. Springer; 2002.

[52] Peyret R. Spectral methods for incompressible viscous flow. Springer; 2002.

[53] Rempfer D. On boundary conditions for incompressible Navier-Stokes problems. Appl Mech Rev 2006;59:107–25.

[54] Karam M, Sutherland JC, Saad T. Low-cost Runge-Kutta integrators for incompressible flow simulations. J Comput Phys 2021;443:110518. http://dx.doi.org/10.1016/j.jcp.2021.110518.

[55] Roe PL. Characteristic-based schemes for the Euler equations. Annu Rev Fluid Mech 1986;18(1):337–65.

[56] Tilton N, Serre E, Martinand D, Lueptow R. A 3D pseudospectral algorithm for fluid flow with permeable walls. application to filtration. Comput & Fluids 2014;93:129–45.

[57] Henriksen P, Hassager O. Simulation of transport phenomena in ultrafiltration. Chem Eng Sci 1993;48(17):2983–99.

[58] Hansen M, Barker V, Hassager O. Spectral element simulation of ultrafiltration. Chem Eng Sci 1998;53(17):3099–115.

[59] Patankar SV. Numerical heat transfer and fluid flow. U.S.: Hemisphere Pub.; 1980.

[60] Cai M, Nonaka A, Bell JB, Griffith BE, Donev A. Efficient variable-coefficient finite-volume Stokes solvers. Commun Comput Phys 2014;16(5):1263–97. http://dx.doi.org/10.4208/cicp.070114.170614a.

[61] Griffith BE. An accurate and efficient method for the incompressible Navier–Stokes equations using the projection method as a preconditioner. J Comput Phys 2009;228(20):7565–95. http://dx.doi.org/10.1016/j.jcp.2009.07.001.

[62] Nangia N, Griffith BE, Patankar NA, Bhalla APS. A robust incompressible Navier-Stokes solver for high density ratio multiphase flows. J Comput Phys 2019;390:548–94. http://dx.doi.org/10.1016/j.jcp.2019.03.042.

[63] Zovatto L, Pedrizzetti G. Flow about a circular cylinder between parallel walls. J Fluid Mech 2001;440:1–25. http://dx.doi.org/10.1017/s0022112001004608.